5-19-2012

Mass fluxes and isofluxes of methane (CH4) at a New Hampshire fen measured by a continuous wave quantum cascade laser spectrometer

Gregory W. Santoni
Harvard University

Ben H. Lee
Harvard University

Jordan P. Goodrich
University of New Hampshire, Durham

Ruth K. Varner
University of New Hampshire, Durham, ruth.varner@unh.edu

Patrick M. Crill
Stockholm University

See next page for additional authors

Follow this and additional works at: https://scholars.unh.edu/faculty_pubs

Recommended Citation

Authors

Gregory W. Santoni, Ben H. Lee, Jordan P. Goodrich, Ruth K. Varner, Patrick M. Crill, J. Barry McManus, David D. Nelson, Mark S. Zahniser, and Steven C. Wofsy

Mass fluxes and isofluxes of methane (CH_4) at a New Hampshire fen measured by a continuous wave quantum cascade laser spectrometer

Gregory W. Santoni,[1] Ben H. Lee,[1] Jordan P. Goodrich,[2] Ruth K. Varner,[2] Patrick M. Crill,[3] J. Barry McManus,[4] David D. Nelson,[4] Mark S. Zahniser,[4] and Steven C. Wofsy[1]

[1]   We have developed a mid-infrared continuous-wave quantum cascade laser direct-absorption spectrometer (QCLS) capable of high frequency (≥ 1 Hz) measurements of $^{12}CH_4$ and $^{13}CH_4$ isotopologues of methane (CH_4) with in situ 1-s RMS $\delta^{13}C_{CH_4}$ precision of 1.5 ‰ and Allan-minimum precision of 0.2 ‰. We deployed this QCLS in a well-studied New Hampshire fen to compare measurements of CH_4 isoflux by eddy covariance (EC) to Keeling regressions of data from automated flux chamber sampling. Mean CH_4 fluxes of 6.5 ± 0.7 mg CH_4 m^{-2} hr^{-1} over two days of EC sampling in July, 2009 were indistinguishable from mean autochamber CH_4 fluxes (6.6 ± 0.8 mgCH_4 m^{-2} hr^{-1}) over the same period. Mean $\delta^{13}C_{CH_4}$ composition of emitted CH_4 calculated using EC isoflux methods was -71 ± 8 ‰ (95% C.I.) while Keeling regressions of 332 chamber closing events over 8 days yielded a corresponding value of -64.5 ± 0.8 ‰. Ebullitive fluxes, representing ~10% of total CH_4 fluxes at this site, were on average 1.2 ‰ enriched in ^{13}C compared to diffusive fluxes. CH_4 isoflux time series have the potential to improve process-based understanding of methanogenesis, fully characterize source isotopic distributions, and serve as additional constraints for both regional and global CH_4 modeling analysis.

1.   Introduction

[2]   Methane (CH_4) is roughly 25 times more effective than carbon dioxide (CO_2) in terms of its integrated greenhouse effect at hundred year timescales [*Lelieveld et al.*, 1998]. After nearly a century of increasing atmospheric mixing ratios, growth rates of atmospheric CH_4 leveled off between 1999 and 2006, stabilizing atmospheric concentrations at ~1.8 μmol/mol [*Lassey et al.*, 2007; *Dlugokencky et al.*, 2009]. Subsequent data, however, suggested renewed growth [*Rigby et al.*, 2008; *Bousquet et al.*, 2011]. These changes in CH_4 concentrations and trends were not predicted [*Montzka et al.*, 2011]. Forward modeling based on emission inventories, reaction rates, OH distributions, and other source and sink parameters have shown limited success in recreating observed spatial distributions over time [*Dlugokencky et al.*, 2003; *Bousquet et al.*, 2006].

[3]   Isotopic measurements of CH_4 can help constrain source and sink uncertainties because processes related to methanogenesis and methanotropy fractionate differently. Isotopic composition, commonly expressed in units of per mil (‰), represents a ratio of two stable isotopes in a sample to that of a standard according to:

$$\delta^{13}C_{sample} = \left(\frac{^{13}C_{sample}}{^{12}C_{sample}} \bigg/ \frac{^{13}C_{vpdb}}{^{12}C_{vpdb}} - 1 \right) \cdot 1000 \qquad (1)$$

where Vienna Pee Dee Belemnite (VPDB) is the international standard for carbon isotopes. Different emission sources have distinguishing isotopic composition. The global mean $\delta^{13}C_{CH_4}$ of tropospheric CH_4 is -47.3 ‰, with interhemispheric differences on the order of 0.2–0.6 ‰ and seasonal variations ranging between 0.1 ‰ and 0.6 ‰ depending on site proximity to CH_4 sources with large seasonal changes in CH_4 flux [*Quay et al.*, 1999; *Miller et al.*, 2002], representing the sum of the flux weighted average of individual CH_4 source isotopic compositions and the mean sink fractionation [*Gierczak et al.*, 1997; *Lassey et al.*, 2000; *Saueressig et al.*, 2001].

[1]Harvard University, School of Engineering and Applied Sciences and Department of Earth and Planetary Sciences, Cambridge, Massachusetts, USA.

[2]Complex Systems Research Center, University of New Hampshire, Durham, New Hampshire, USA.

[3]Department of Geological Sciences, Stockholm University, Stockholm, Sweden.

[4]Center for Atmospheric and Environmental Chemistry, Aerodyne Research, Inc., Billerica, Massachusetts, USA.

Corresponding author: G. W. Santoni, Department of Earth and Planetary Sciences, Harvard University, 24 Oxford St., Cambridge, MA 02138, USA. (gsantoni@gmail.com)
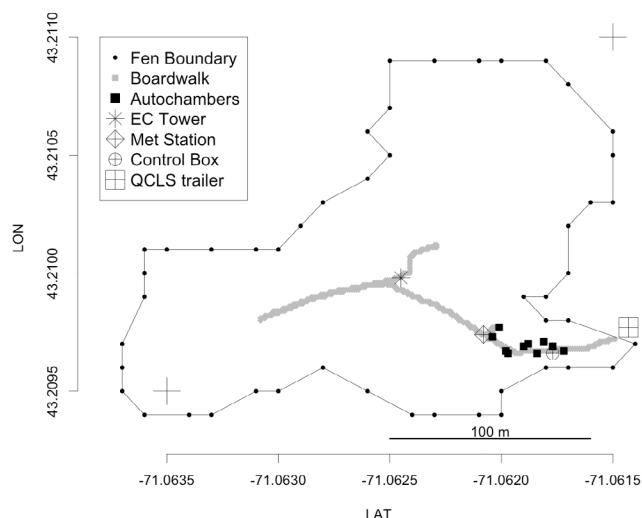
Figure 1. Location of the QCLS relative to the EC tower and autochambers at Sallie's Fen. Waypoints for the edge of the fen are shown in black. Land surrounding the fen is largely forested with Red Maple. The two hatches show the lower-left and upper-right points corresponding to the axis hash marks.

[4] The utility of isotopic characterization is limited by cumbersome measurement methods. $\delta^{13}C_{CH_4}$ measurements typically involve taking flask samples in the field and returning the flasks to a facility for analysis. Isotopic composition is determined by using a gas chromatograph (GC) to separate out CH_4, a combustor (C) to fully oxidize CH_4 to CO_2 and an Isotope Ratio Mass Spectrometer (IRMS) to measure the $^{13}C_{sample}/^{12}C_{sample}$ ratio of that CO_2. High accuracy can be achieved: GC-C-IRMS has reported precision of ~0.1 ‰ with 0.2 L of air [*Miller et al.*, 2002] and even better precisions of <~0.05 ‰ for larger volumes of air (order ~10 L) are achieved with 'off-line' techniques [*Lowe et al.*, 1991]. Samples, however, are cumbersome to obtain, expensive to analyze, and require large masses of CH_4 and consequently large sample volumes for atmospheric measurements. Long-term continuous measurements in remote areas are impractical, and consistent monitoring of source composition is costly and labor intensive.

[5] Significant research has focused on the development of laser-based absorption spectrometers to measure the isotopic composition of various tracers such as H_2O [*Dawson et al.*, 2002; *Gupta et al.*, 2009], CO_2 [*Crosson et al.*, 2002; *Bowling et al.*, 2003; *Griffis et al.*, 2008; *McManus et al.*, 2005, 2010], CH_4 [*Kosterev et al.*, 1999; *Zahniser et al.*, 2009; *Witinski et al.*, 2011] and N_2O [*Waechter et al.*, 2008; *Mohn et al.*, 2010]. This technique generates continuous high frequency data and is readily usable at long-term monitoring sites. Such instrumentation has inspired the concept of CO_2 isofluxes – isotopically weighted CO_2 fluxes derived from isotopic mass balance – using eddy covariance (EC) techniques, useful in partitioning between respiration and photosynthesis and determining source isotopic composition of CO_2 [*Baldocchi and Bowling*, 2003; *Knohl and Buchmann*, 2005; *Saleska et al.*, 2006; *Griffis et al.*, 2008].

[6] We present the first in situ ambient CH_4 isoflux measurements by EC sampling using a tunable quantum cascade

laser direct-absorption spectrometer (QCLS) at Sallie's Fen, a research fen in New Hampshire. We divide the isoflux measurements of CH_4 by the mass flux measurements of CH_4 to derive the isotopic composition of CH_4 emitted from the fen. Using the QCLS to subsample an established automatic flux chamber network (autochambers) distributed throughout the fen, we compare Keeling plot regressions of the autochamber data to derived $\delta^{13}C_{CH_{4source}}$ values from EC isoflux methods in order to further characterize the isotopic source composition of CH_4 emissions from the fen. Potential improvements to instrumentation, sample conditioning, calibration, and data post-processing are discussed.

2. Site Description

[7] Sallie's Fen is a *Sphagnum*-dominated peatland located in southeastern New Hampshire near the University of New Hampshire (43° 12.5′ N, 71° 03.5′ W). It is a mineral poor 1.7 ha fen with a peat depth range of 2–4.5 m. Ten automated Lexan flux chambers (autochambers) were interspersed in various plant communities in the fen and have been in operation since 2000. The chamber system and fen characterization is described in more detail by *Bubier et al.* [2003]. Figure 1 shows the distribution of the chambers in the fen, the boundary between the fen and surrounding forested lands and farms, the location of the EC tower sampling location, and the location of the QCLS during sampling. Ongoing measurements since 1989 have characterized gas exchange [*Carroll and Crill*, 1997; *Bubier et al.*, 2003], seasonality [*Melloh and Crill*, 1996; *Treat et al.*, 2007], vegetation [*Frolking and Crill*, 1994], and isotopic composition of carbon in CO_2 [*Shoemaker and Schrag*, 2010]. Yearlong autochamber measurements from 2009 have used a Los Gatos Research (LGR) Integrated Cavity Output Spectrometer (ICOS) to record both CH_4 and CO_2 fluxes from the autochambers [*Goodrich et al.*, 2011].

3. Instrumentation

3.1. Quantum Cascade Laser Spectrometer (QCLS)

[8] Infrared absorption spectroscopy is a widely used technique based on the Beer-Lambert law to quantify trace gas concentrations using frequency-specific light absorption by individual molecules associated with ro-vibrational transitions. Advances in laser sources [*Faist et al.*, 1994], detectors [*Nelson et al.*, 2004], and multipass cells [*McManus et al.*, 1995] have allowed for increased sensitivity [*Tuzson et al.*, 2008; *McManus et al.*, 2010] and high frequency measurements [*Zahniser et al.*, 1995] of chemical species, and their stable isotopes, with low ambient concentrations.

[9] In our sensor, a room temperature, mid-infrared, continuous-wave quantum cascade laser (QCL, Alpes Lasers) was housed in a hermetically sealed box, and its temperature (−14°C) and output frequency were controlled by a Peltier element in the box coupled to a recirculating chiller. Output power of the QCL was ~30 mW. The output frequency was coarsely maintained by controlling the laser temperature while fine adjustments to the output frequency were made by modulating the current with a high-compliance source (ILX Lightwave 3232). Current to the QCL was linearly ramped, scanning the laser frequency across 480 channels at a rate of 909 kHz. The scan included absorption lines for $^{12}CH_4$,
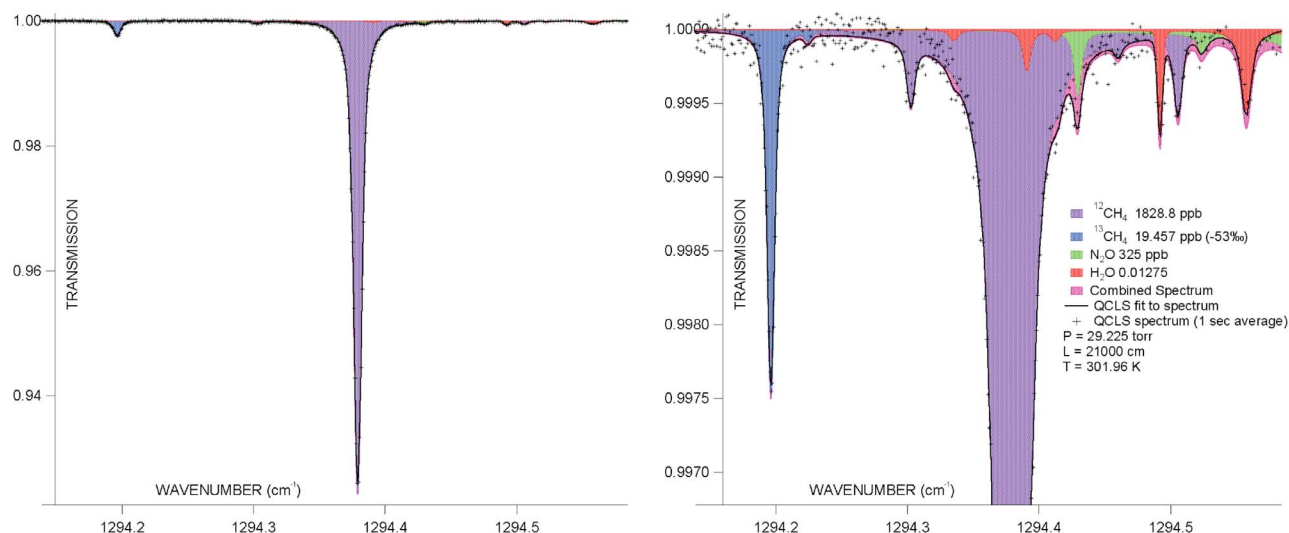
Figure 2. (left) A 1-s QCLS spectrum (pluses) of the 520 channels tuned across with the QCL along with the TDLWintel fit to the spectrum (black line), and a simulated HITRAN spectrum using the measured pressure, temperature, absorbing species (colors), and an instrumental line width of 0.001 cm^{-1}. (right) Close-up of the spectrum focusing on the $^{13}CH_4$ line.

$^{13}CH_4$, N_2O, and H_2O in the 1294.1 to 1294.4 cm^{-1} region. The current supplied to the laser dropped below lasing threshold for an additional 40 channels during each scan so that a background 'zero-light-level' (detector output) was measured. This ramped current and shutoff pulse sequence was controlled by TDL Wintel ® software. A total scan of 520 channels took $5.72 \cdot 10^{-4}$ seconds. Because the laser frequency did not respond linearly to the ramped current supplied to the laser, the laser frequency tuning rate was determined by fitting the spectrum of the system with a Germanium etalon in the beam path. The instrumental half-width at half-maximum (HWHM) line width for the laser was <0.001 cm^{-1}, negligible compared to the molecular absorption line width.

[10] Light from the QCL was directed into an astigmatic multipass sampling cell operated at low pressure (<7 kPa) and detected by a thermoelectrically cooled detector. A long effective path length (210 m) was required to achieve sufficient precision on the $^{13}CH_4$ line and achieved using 238 passes between mirrors spaced 88.23 cm apart. During EC measurements, a TriScroll 600 l/min pump (Varian TriScroll600) generated a flow rate of ~11 slpm through the 5 L sample cell at 4.0 kPa, corresponding to a cell time constant of 1.08 s.

[11] Mixing ratios were derived by TDL Wintel ® at ~1 s intervals using a Levenberg-Marquardt least squares fit to each sample spectrum. The fitting procedure treated each spectral line as a Voigt profile taking into account the line strength, line location, air broadening coefficient, pressure, and temperature. A sample ~1 s spectrum representing the average of 1748 scans across the 480 channels is shown in Figure 2 along with the fit to the spectrum and a simulation using HITRAN line parameters and measured temperature, pressure, and mixing ratios. The baseline level (I_o in the Beer-Lambert law) was modeled as a low-order polynomial. The fitting algorithm took ~115 ms, making ~8 Hz

measurements possible, but not independent on account of the cell time constant.

[12] Removal of absorbance in the external path and baseline flattening was achieved by background subtraction using CH_4-free air as determined with the QCLS spectra. Middlesex Gases 0.0001 Ultra Zero Air was passed through the sample cell and an average background spectrum was acquired over 20 s. Sample spectra were normalized by dividing by the mean of bracketing background spectra [*Nelson et al.*, 2004].

[13] Figure 3 shows an in-field time series of $^{12}CH_4$, $^{13}CH_4$, and their ratio expressed as $\delta^{13}C_{CH_4}$ for 30 min of sampling from a calibration tank. The $^{12}CH_4$ and $^{13}CH_4$ axes are each scaled by their relative abundance according to HITRAN, 0.0111031 and 0.988274, respectively, to illustrate the factor of ~6 greater noise on the $^{13}CH_4$ absorption line. Precision as a function of integration time gives a 1-s RMS $\delta^{13}C_{CH_4}$ precision of 1.5 ‰ $Hz^{-1/2}$. The Allan minimum reaches <0.2 ‰ $Hz^{-1/2}$ at order 10^2 seconds, approaching the precision of GCC-IRMS methods. In order to compare instruments measuring different tracers, it is useful to express performance as absorption precisions, which relate measurement precisions to line strengths and ambient mixing ratios [*Nelson et al.*, 2002]. The absorption precisions for $^{13}CH_4$ and $^{12}CH_4$ are $4.5 \cdot 10^{-6}$ $Hz^{-1/2}$ and $1.5 \cdot 10^{-5}$ $Hz^{-1/2}$, respectively, determined using the corresponding line center absorbances of 0.25% and 8% calculated in the spectral simulation (Figure 2) and the 1 Hz Allan precisions at atmospheric abundance. Absorption precision on the major isotopologue ($^{12}CH_4$) is worse than for $^{13}CH_4$ because the measurement of the $^{12}CH_4$ is limited by noise proportional to its peak absorbance, a factor of 36 times greater than that of the $^{13}CH_4$.

[14] Density fluctuations associated with water vapor fluxes are a concern for gas sampling systems because of the potential need for Webb-Pearlman-Leuning (WPL) corrections [*Webb et al.*, 1980]. Because of the fast flow rates and
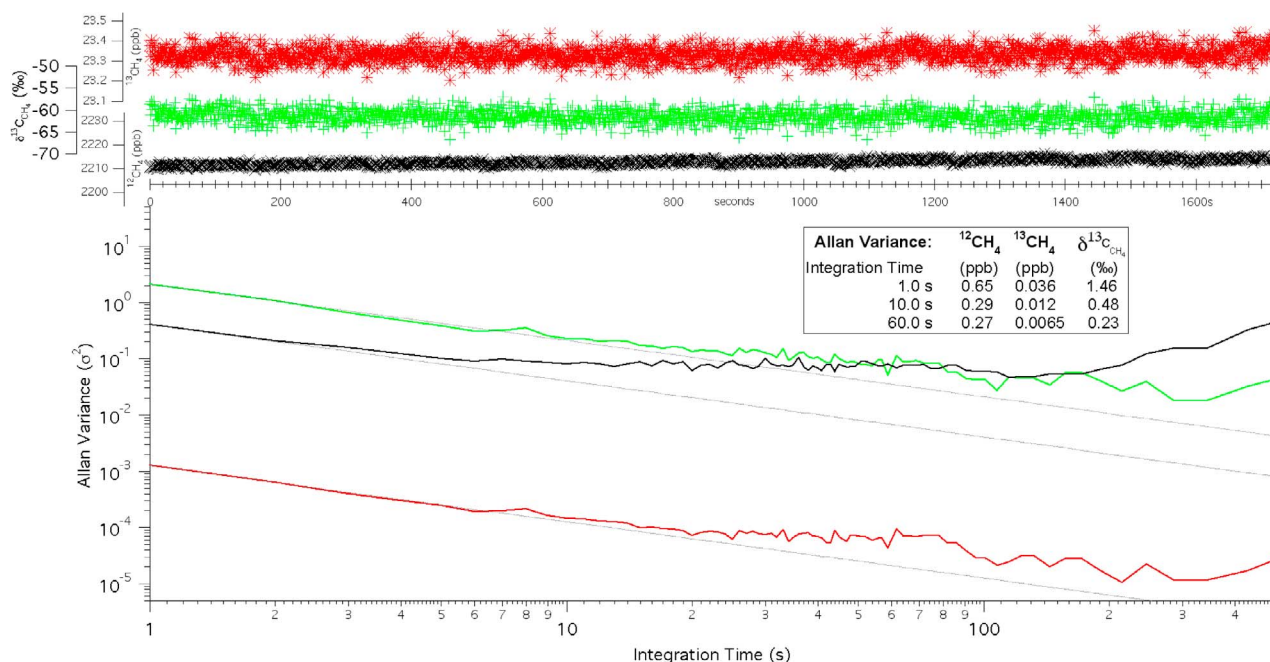
Figure 3. Time series and Allan variance plot of $^{12}CH_4$ (black), $^{13}CH_4$ (red), and $\delta^{13}C_{CH_4}$ (green). Data were taken over 45 min with 45 s background ultra-zero air spectra taken every 3 min. The axes for $^{12}CH_4$ and $^{13}CH_4$ each represent 40 ppb once scaled by the HITRAN isotopic abundances, 0.0111031 and 0.988274, respectively [*De Biévre et al.*, 1984]. This illustrates the factor of ~6 larger noise on the $^{13}CH_4$ absorption line. The Allan variance for each time series is plotted along with the white-noise variance, showing that the $\delta^{13}C_{CH_4}$ measurement precision at minute-long timescales, 0.23 ‰, approaches the precision of GC-C-IRMS methods.

large sample volumes during EC measurements, drying the sample was impractical. Instead, the QCLS scan was expanded to include an additional 40 channels to measure water content using a nearby absorption line seen in Figure 2. *Tuzson et al.* [2010] used a similar instrument to show that in addition to density corrections, line broadening effects due to water vapor accounted for an additional correction of 16% of the total WPL correction. This additional correction is non-negligible in certain applications such as EC observations above areas of low CH_4 flux. Tests using calibrated cylinder air run through a water-bubbler to generate air with varying H_2O mixing ratios showed that H_2O content did not modify the isotopic measurements since the line broadening effects were close to identical for both isotopologues.

3.2. Autochamber and Eddy Covariance Measurements

[15] The QCLS, calibration tanks, and other peripherals were located in an enclosed 6′ by 8′ trailer at the edge of the fen, approximately 40 m from the autochambers. The autochambers consisted of 10 chambers with closed loops of 3/8″ OD Synflex (Dekaron) tubing and total loop lengths ranging from 10–30 m depending on the chamber location relative to the valve manifold control box (Figures 1 and 4). A two-stage diaphragm pump drew ~10 slpm of air through the autochambers in a closed loop via the valve manifold, spending 18 min on each individual chamber for a total autochamber sampling cycle of 180 min. Individual autochambers

were automatically closed and opened at minutes 6 and 12, respectively, during which time a flux was calculated. Minutes 0–6 and 12–18 of a given 18 min cycle flushed the system with ambient air while the autochamber lid was open to the atmosphere. Measurements of CO_2 and CH_4 at 12 s intervals were obtained using the LGR-ICOS which subsampled ~2 slpm from the main ~10 slpm draw [*Goodrich et al.*, 2011]. During autochamber subsampling, a second closed loop of 80 m using 1/4″ OD Synflex tubing brought air to the QCLS from the main ~10 slpm autochamber flow (Figure 4). A 4-stage low pressure pump (Vaccubrand MD-4) was used to achieve a 2.5 slpm flow through the 5 L QCLS sampling cell volume at 5.3 kPa. A Licor (LI-7000) was positioned upstream in series of the QCLS and recorded CO_2 and H_2O at 1 Hz using a CO_2-calibrated dry tank as the reference. Calibration additions were done upstream of the Licor and involved an additional solenoid valve to control return flow from the pump to the main autochamber draw so as not to return tank air to the main autochamber draw.

[16] The EC sampling location was positioned in the center of the fen, approximately 100 m from the QCLS. A sonic anemometer (Campbell CSAT-3) was mounted on a 3 m tower such that the sonic head was 2.0 m above the peat surface and oriented facing into the predominant wind-direction (N-NE). A sample inlet consisting of two 1-micron filters connected in parallel (to minimize the pressure drop across the filter and decrease the likelihood of blockage) was located 2.0 m above the peat surface and 0.2 m downwind from the CSAT head. The vegetation canopy was roughly
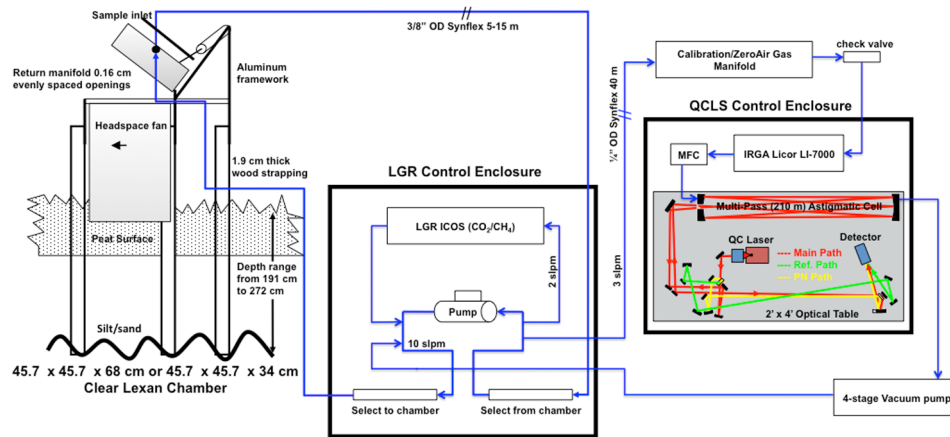
Figure 4. Autochamber system depicted by *Bubier et al.* [2003] showing the sample flow (blue arrows) for both QCLS and LGR subsampling from the main autochamber loop. The subsamples for both the LGR and QCLS are returned to the main autochamber loop downstream of the main autochamber pump (middle) and individual chambers are selected sequentially on an 18-min-per-chamber cycle.

0.3 m above the peat surface. To minimize the pressure drop associated with a 100 m long sampling line, 1/2″ OD synflex tubing was used, requiring a 26 slpm flow to maintain fully turbulent conditions ($R_e \sim 4000$), and resulting in a pressure drop of only 3.3 kPa from the EC sampling inlet to the QCLS.

[17] To avoid wasting calibration gases associated with high flows during EC sampling, tank air was introduced upstream of the QCLS through a manifold equipped with a diaphragm check valve to reduce excess regulator pressure down to atmospheric pressure. During tank air additions the mass flow controller maintained instantaneous cell pressure fluctuations to within ~ 100 Pa of sampling pressure, which stabilized within 2 s of switching from sample to calibration gas. A second two-head diaphragm pump (KNF Neuberger Model UA0026.1) pulled ~ 13 slpm through the Licor measuring H_2O and CO_2 at 5 Hz. The cell volume of the Licor is 10.86 cm^3, resulting in a sample cell time constant of 0.086 s. The ~ 11 slpm QCLS draw (Section 3.1), the ~ 13 slpm Licor draw, and a third draw of ~ 7 slpm were connected in parallel for a total flow of ~ 31 slpm through the main 100 m sampling line. This configuration, shown in Figure 5, minimized tank air consumption, ensured a ~ 1 s

response time, and maintained turbulence at the inlet even during tank-air additions to the QCLS.

[18] A data logger (Campbell CR-10 with new PROM for CSAT-3 sonic commands) located at the base of EC tower recorded wind velocities and sonic temperatures from the sonic anemometer at 8 Hz as well as air and water temperatures from two thermistors at 1 Hz. A PC in the instrument enclosure periodically collected data from the data logger via a short-haul modem (Campbell RAD-5). Unfortunately, data transfers every 3 min resulted in corruption of the CSAT data with spurious time-stamps. Exclusion of these artifacts resulted in the loss of 34% of the sonic data over the EC measurement period. The PC logging the CR-10 data also serially recorded the Licor data and was networked and time-synchronized to the QCLS computer.

4. Methods

4.1. QCLS Calibrations

[19] QCLS accuracy depended largely on the calibration procedure and the stability of the background laser spectrum in the absence of absorbing species. Ultra-zero air was introduced to the sampling cell every 10 min (background
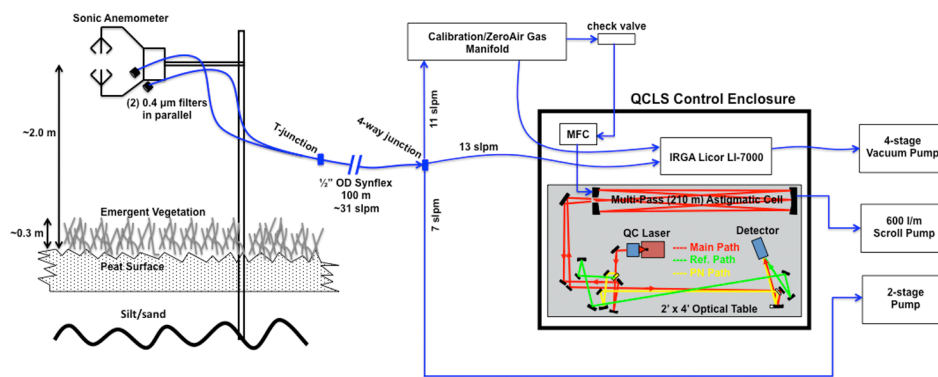

Figure 5. Eddy Covariance setup and flow diagram during QCLS isoflux measurements. Sample flow is shown in blue arrows, originating by the EC tower in the middle of the fen. Three pumps (right) draw through various instruments to maintain fully turbulent conditions throughout the sampling system.

subtraction) in order to capture the influence on the baseline of small temperature and pressure variations that occurred over diurnal timescales. Calibrations were done using pairs of tanks that spanned the observed atmospheric range of CH_4 above the fen, notably ∼1.8 to ∼10 μmol/mol, the latter of which was regularly observed during summer/fall nighttime inversions. During EC measurements, a low-span (LS, ∼1.8 μmol/mol) tank was sampled every 10 min and a high-span (HS, ∼10 μmol/mol) tank every 3 h. This was done because the LS tank was closer to ambient concentration and therefore had a greater influence on the calibration interpolation applied to the data. During autochamber measurements, when fluxes inside a closed chamber induced consistently higher mixing ratios, HS and LS tanks were alternately sampled every 18 min, coincident with the autochamber cycle. A cubic spline was interpolated to the $^{12}CH_4$ and $^{13}CH_4$ mixing ratios for both the HS and LS tanks. Each isotopologue of CH_4 was treated as an independent measurement, separately calibrated. The range of variation of mixing ratios of CH_4 obtained from spectral parameters only for one particular calibration tank over the course of a day, normalized by the atmospheric abundance of each, was roughly 30 ppb or 1.6%. The cubic spline interpolations versus time for $^{12}CH_4$ and $^{13}CH_4$ tracked each other well, largely because diurnal temperature variations affected each line similarly. The LS and HS tanks were calibrated to the VPDB scale by means of duplicate subsampled flasks of all calibration cylinders which were analyzed offline by means of GC-C-IRMS at Woods Hole Oceanographic Institute. Calibrated tank values for χ_{CH_4} were given by Scott Specialty Gases at 1% accuracy (i.e., ±18 nmol/mol for a ∼1.8 μmol/mol LS tank and ±100 nmol/mol for a ∼10 μmol/mol HS tank) and confirmed using the QCLS and spectroscopic parameters (line strength, pressure, temperature, broadening coefficients, etc.). QCLS mixing ratios of total CH_4, $^{12}CH_4$, and $^{13}CH_4$ acquired by spectral fitting were then linearly interpolated to the cubic spline calibration interpolations, putting them on the VPDB scale. The interpolation was calculated as:

$$\chi_{^{12}CH_4} = \left(\frac{\chi_{^{12}CH_{4,QCLS}} - \chi_{^{12}CH_{4,LS,spl}}}{\chi_{^{12}CH_{4,HS,spl}} - \chi_{^{12}CH_{4,LS,spl}}} \right) \cdot \left(\chi_{^{12}CH_{4,HS,cal}} - \chi_{^{12}CH_{4,LS,cal}} \right)$$
$$+ \chi_{^{12}CH_{4,LS,cal}} = \chi_{CH_4} \cdot A_{HITRAN_{12}CH_4} \tag{2}$$

$$\frac{\chi_{^{13}CH_4}}{\left(^{13}C_{vpdb} / ^{12}C_{vpdb} \right)} = \left(\frac{\chi_{^{13}CH_{4,QCLS}} - \chi_{^{13}CH_{4,LS,spl}}}{\chi_{^{13}CH_{4,HS,spl}} - \chi_{^{13}CH_{4,LS,spl}}} \right)$$
$$\cdot \left[\chi_{^{12}CH_{4,HS,cal}} \cdot \left(1 + \frac{\delta^{13}C_{CH_{4,HS,vpdb}}}{1000} \right) \right.$$
$$\left. - \chi_{^{12}CH_{4,LS,cal}} \cdot \left(1 + \frac{\delta^{13}C_{CH_{4,LS,vpdb}}}{1000} \right) \right]$$
$$+ \chi_{^{12}CH_{4,LS,cal}} \cdot \left(1 + \frac{\delta^{13}C_{CH_{4,LS,vpdb}}}{1000} \right) \tag{3}$$

where $\chi_{^{12}CH_{4,QCLS}}$ and $\chi_{^{13}CH_{4,QCLS}}$ represent the 1 Hz dry air mixing ratios calculated by TDL Wintel ®, $\chi_{^{12}CH_{4,HS,spl}}$ and $\chi_{^{13}CH_{4,HS,spl}}$ the high-span spline interpolations to the $^{12}CH_4$

and $^{13}CH_4$ mixing ratios calculated by TDL Wintel ® from retrieved absorbance during the calibration tank additions, $\chi_{^{12}CH_{4,LS,cal}}$ and $\chi_{^{12}CH_{4,HS,cal}}$ the calibrated mole fraction values for the LS and HS tanks respectively, and $\delta^{13}C_{CH_{4,LS,vpdb}}$ and $\delta^{13}C_{CH_{4,LS,vpdb}}$ the GC-C-IRMS calibrated isotopic composition of the LS and HS tanks, respectively. The ratio of $\chi_{^{13}CH_4}$ to $\chi_{^{12}CH_4}$ computed using equations (3) and (2), respectively, represents the quantity $\frac{^{13}C_{sample}}{^{12}C_{sample}}$ and can be expressed in ‰ notation according to equation (1). The total mole fraction of CH_4, χ_{CH_4}, is determined using equation (2) and the HITRAN isotopic abundances for the dominant isotopologue of CH_4, $A_{HITRAN_{12}CH_4}$ [De Biévre et al., 1984].

4.2. Eddy Covariance Data Processing

[20] Continuous EC data were obtained on 18–19 July 2009. The CH_4 flux was calculated from the covariance of χ'_{CH_4} and w′, the fluctuating parts of the CH_4 mixing ratio and vertical wind velocity, respectively. Adopting the notation of Saleska et al. [2006], we define the CH_4 flux as:

$$F_{CH_4} = \rho \overline{w'\chi'_{CH_4}} \tag{4}$$

where ρ represents the density of the sample, the overline represents the covariance of the two quantities, and the primes in the covariance term are fluctuations from the mean using Reynolds decomposition. Derivation of the isoflux has been presented by Saleska et al. [2006] and Griffis et al. [2008] who both focus on isofluxes of CO_2 as a means of partitioning photosynthesis and respiration. The analog of equation (4) for isofluxes of CH_4 is:

$$\delta^{13}C_{CH_{4source}} \cdot F_{CH_4} = \rho \overline{w' \left(\delta^{13}C_{CH_4} \cdot \chi_{CH_4} \right)'} \tag{5}$$

where $\left(\delta^{13}C_{CH_4} \cdot \chi_{CH_4} \right)'$ is the fluctuating part of the Reynolds decomposition of the product of $\delta^{13}C_{CH_4}$, calculated from equations (1)–(3), and χ_{CH_4}, the calibration corrected mixing ratio from equation (2). We estimate the isotopic source composition of CH_4 from the fen, $\delta^{13}C_{CH_{4source}}$, by dividing equation (5) by equation (4). Isotopic data from the autochambers do not exist for these two days, but comparisons to Keeling plots were made with QCLS autochamber data later in the summer.

[21] Non-sonic scalars were measured ∼100 m from the EC tower at the QCLS trailer. Lag-times were determined by maximizing the covariance of each scalar (χ'_{CH_4}, χ'_{CO_2}, χ'_{H_2O}, etc.) with w′ as a function of Δt over 100 s intervals. 42 of the 96 half-hour intervals with u* > 0.1 m/s and a clearly identifiable maximum/minimum covariance in the lagged covariance plot were linearly interpolated to determine the sampling lag time (typically ∼6–8 s) through the tubing for each half-hour time segment. The standard deviation of the covariances of the first and last 20 s of the 100 s interval is reported as measurement error, a method often used for closed-path sensors [Wienhold et al., 1994; Kormann et al., 2001; Smeets et al., 2009]. Other relevant quantities calculated have been summarized elsewhere: Kormann et al. [2001] provide a detailed overview of the important quantities, Smeets et al. [2009] discuss CH_4–specific EC calculations, and both Webb et al. [1980] and Ibrom et al. [2007a] discuss WPL corrections.
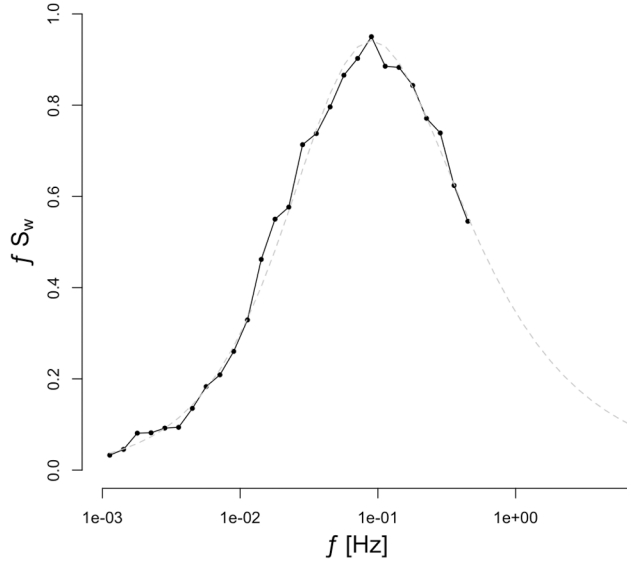
Figure 6. The vertical wind velocity (w') spectrum from the 2 m tower using the power spectrum of 57 of the 96 half-hour intervals (two days) calculated by Lomb-Scargle methods (black) and the predicted Kaimal curve (gray) [*Kaimal and Finnigan*, 1994; *Lee et al.*, 2004] for a slightly unstable atmosphere.

[22] We performed two coordinate rotations to force the mean horizontal and vertical winds to zero. Rotation of the vertical axis resulted in a mean angle of rotation for the 96 half-hourly segments of 0.56° with a 95% CI of 1.1°. EC averaging time was set to be 30 min, long enough to capture the fast and slow eddies up to the spectral gap beyond which diurnal and synoptic variability influenced the power spectrum of winds, momentum, and heat flux. Spectral analysis showed that the ogives – the cumulative power densities of the cospectra – of our flux data asymptote well before frequencies associated with 30 min [*Lee et al.*, 2004]. Because of the gaps in the data every 3 and 10 min associated with data logger transfers and calibrations, respectively, Lomb-Scargle methods were used instead of traditional spectral analysis to compute cospectra [*Press et al.*, 1992].

[23] The frequency spectrum of w' for 57 of the 96 half-hour intervals over the two days, each having a friction velocity ($u*$) greater than 0.1 m/s is shown in Figure 6. Relevant cospectra calculated by Lomb-Scargle methods are shown in Figure 7 and represent half-hour averages with power averaged into exponentially increasing frequency bins. The spectra are approximated by the model [*Lee et al.*, 2004]:

$$f \cdot S(f) = \frac{A \cdot \left(f/f_x\right)}{\left[1 + m\left(f/f_x\right)^{2\mu}\right]^{\frac{1}{2\mu}\left(\frac{m}{m+1}\right)}} \qquad (6)$$

where A is a normalization parameter, f_x is the frequency at which the frequency-weighted power co/spectrum reaches a maximum (here 0.09 Hz for w' and $w'T'$, and 0.064 Hz for $w'\chi'_{CH_4}$), μ is a broadness parameter (here 2/3, consistent with a slightly unstable atmosphere), and m is set to 3/2 for

spectra and 3/4 for cospectra to describe the $-5/3$ and $-7/3$ power laws in the inertial subrange, respectively. Peak power was well predicted by the Kaimal curve for the spectra using a measurement height of 2.0 m, a vegetation height of 0.3 m, and a mean horizontal wind velocity of 0.45 m/s [*Kaimal and Finnigan*, 1994]. Cospectra in Figure 7, approximated from equation (6) with m = 3/4, show some evidence of differential spectral attenuation and illustrate the different eddy length scales responsible for the fluxes of the different scalars.

[24] We calculated CH_4 fluxes and isofluxes from equations (4) and (5) using two methods: WPL corrected fluxes and dry-mole fraction fluxes. The first used the water vapor measurement of the Licor and applied WPL corrections to the wet-mole fraction CH_4 fluxes. The second used the QCLS water measurement to correct the $^{12}CH_4$ and $^{13}CH_4$ mixing ratios to dry-mole fraction. The two methods produced statistically indistinguishable results at the p = 0.05 level and the latter method is presented in the results. Because measurements such as χ'_{CH_4} and χ'_{CO_2} did not occur at frequencies as high as that of the sonic anemometer, degradation of the $\overline{w'T'_v}$ cospectrum (vertical wind velocity and sonic virtual temperature) from 8 Hz 'raw' data to 5 Hz Licor and 1 Hz QCLS data was used to calculate the correction factor for high-frequency loss [*Ibrom et al.*, 2007b] according to:

$$F_1 = \frac{\overline{w'T'_{v_{raw}}}}{\overline{w'T'_{v_{sample}}}} \qquad (7)$$

For Licor sampling at 5 Hz, the mean F_1 was 100.05 ± 0.85 (95% C.I.) % showing that the high-frequency loss due to degradation of an 8 Hz signal into a 5 Hz was negligible.
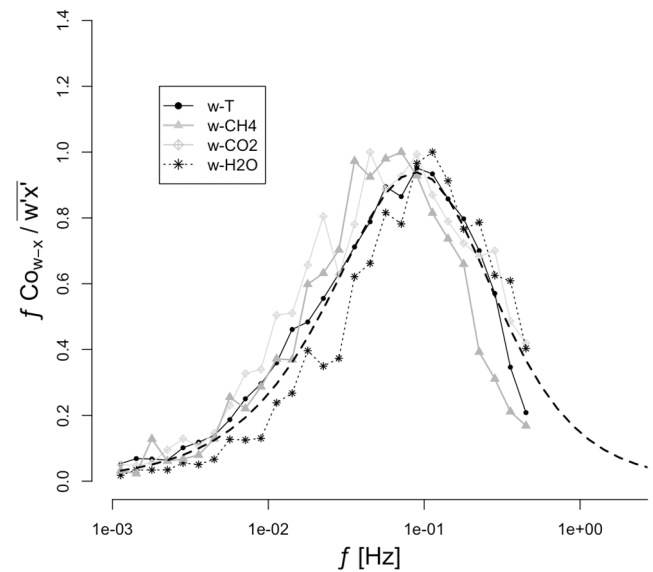

Figure 7. Various cospectra calculated from Lomb-Scargle methods. Cospectra are multiplied by the frequency and normalized by the half-hourly covariance and represent the mean of the 57 half-hour intervals with $u* > 0.1$ m/s. The predicted cospectrum for $w'T'$ is shown as a smooth black dashed line [*Lee et al.*, 2004].
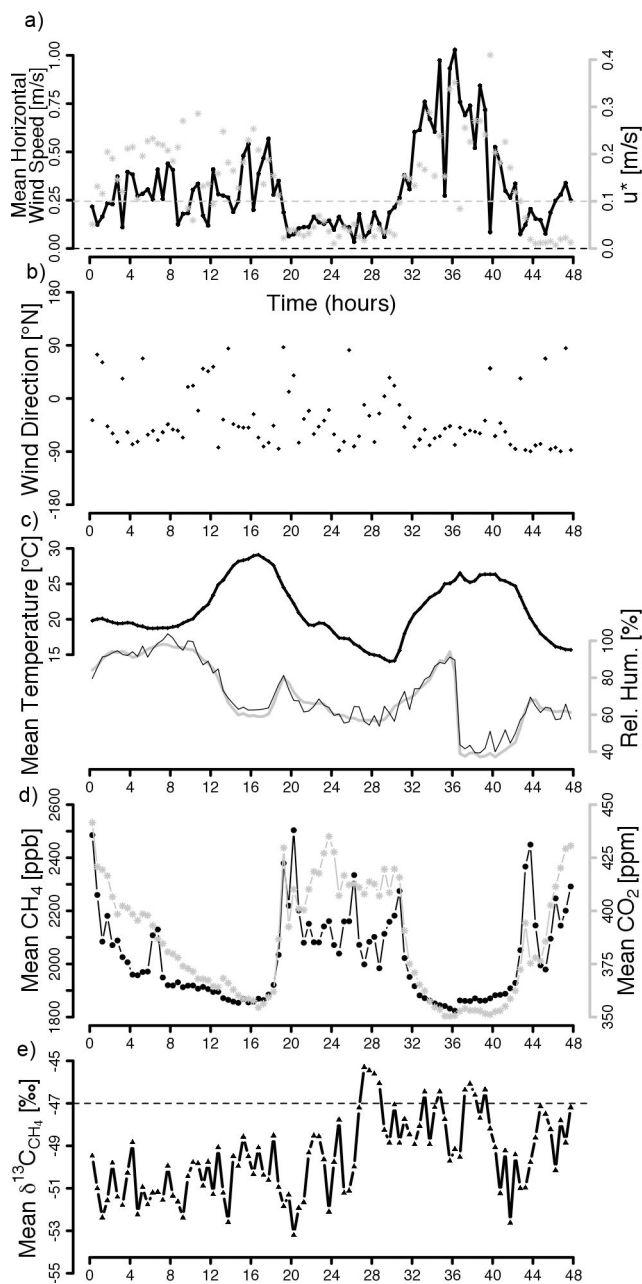
Figure 8. Time series of EC half-hourly averages over 18–19 July 2009 of (a) mean horizontal wind speed (black) and u* (gray) where the dashed gray line is the u* threshold of 0.1 m/s used as a filter, (b) wind direction, (c, left) air temperature, (c, right) relative humidity shown calculated using the Licor H_2O measurement (gray) and using the QCLS H_2O measurement (thin black), (d) mean mixing ratios of CH_4 (black) and CO_2 (gray), and (e) mean $\delta^{13}C_{CH_4}$ where the dashed black line in represents −47 ‰, the mean isotopic composition of ambient CH_4 in the free troposphere.

Correction factors for high frequency loss of CO_2 and H_2O fluxes were therefore not applied to the data. The corresponding high frequency correction factor for the 1 Hz QCLS data was 92.87 ± 6.59% indicating a loss of ~7% of

the covariance at high frequency. We corrected for this loss using equation (7), substituting CH_4 for T_v and rearranging, to solve for the true covariance as [*Ibrom et al.*, 2007b; *Kroon et al.*, 2007]:

$$\overline{w'\chi'_{CH_4}} = \frac{1}{F_1} \cdot \left(\overline{w'\chi'_{CH_{4@1Hz}}} \right) \tag{8}$$

Horst [1997] calculate F_1 using spectral transfer function analysis according to $F_1 = 1 + (2\pi f_m \tau_c)^\alpha$ where f_m represents the peak of the logarithmic cospectrum (0.064 Hz for χ_{CH_4}), τ_c represents the time constant of the sensor (1.08 s for the QCLS), and α =7/8 for neutral and unstable stratification within the surface-flux layer, giving a high frequency attenuation correction factor of 1.48, much larger than the correction factor derived from equation (7).

4.3. Autochamber Data Processing

[25] Eighty autochamber closures per day were observed by the QCLS data over eight days (12–13, 28–31 August 2009, 1–2 September 2009). Each chamber closing was treated as an independent measurement of (a) the CH_4 flux, calculated from chamber ground temperature (T_{ground}), volume ($V_{chamber}$), surface area ($A_{chamber}$), and a regression of the CH_4 time series using a Type I simple linear regression (SLR, e.g., blue lines on the left of Figure 10) according to:

$$F_{CH_4} = \frac{\Delta\chi_{CH_4}}{\Delta t} \cdot \left(\frac{M_{CH_4} P_{ground} V_{chamber}}{R T_{ground} A_{chamber}} \right), \tag{9}$$

where R is the ideal gas constant, and M_{CH_4} is the molecular mass of CH_4, and (b) isotopic source composition for that chamber, $\delta^{13}C_{CH_{4source}}$, derived from the y-intercept of a Keeling plot (e.g., x =0 on the right side of Figure 10) in which $\delta^{13}C_{CH_4}$ is plotted against $1/\chi_{CH_4}$. The regression is a mixing line assuming two end-members: CH_4 from the fen and atmospheric CH_4. In this case, Type II regressions which use independent error constraints on ordinate and abscissa variables were indistinguishable from Type I regression because the measurement error on $1/\chi_{CH_4}$ was negligible compared to the measurement error of $\delta^{13}C_{CH_4}$.

[26] Of the 640 chamber closings observed with the QCLS, 585 were used to calculate fluxes and isotopic composition; 217, 139, and 229 of which were categorized as linear, ebullitive, and random fluxes, respectively. Linear buildups were defined as having residual variances on the flux regression <0.05 nmol/mol/s. CH_4 fluxes both by diffusion from the water surface and by plant mediated transport exhibited linear buildups of CH_4 in chambers whereas ebullitive fluxes showed sudden jumps, categorized by a CH_4 flux regression >8 nmol/mol/s that were between 10 and 120 s in duration as defined in *Goodrich et al.* [2011]. In order to differentiate the isotopic composition of ebullitive fluxes in the autochambers, Keeling regressions using the ebullitive events were compared to the Keeling regression of the entire flux interval using 83 definitive ebullitive events which lasted between 10 and 60 s. Random buildups showed oscillations in the CH_4 time series having amplitudes >50 nmol/mol, a result of improper sealing of the
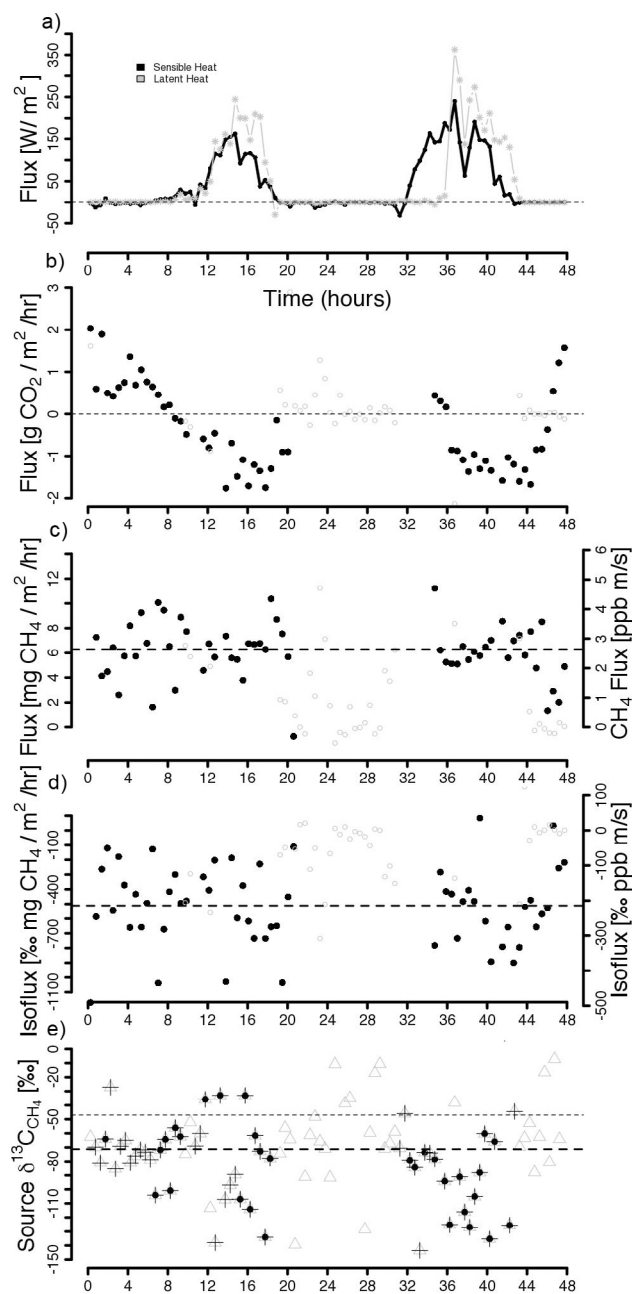
Figure 9. Time series of EC half-hourly (a) sensible and latent heat fluxes, (b) CO_2 fluxes, where the thin dashed black line denotes the transition from positive to negative NEE and light gray circles represent fluxes not used in the analysis because they correspond to half-hour intervals with $u^* < 0.1$ m/s, (c) CH_4 fluxes where the thick dashed black line denotes the average over the two days, and (d) CH_4 isofluxes. For Figures 9c and 9d, two different scales are used on the left and right axes. (e) The time series of the resulting source isotopic composition of CH_4 derived from the measurements, $\delta^{13}C_{CH_{4source}}$ is shown for n = 90 (gray triangles), n = 55 (thin black pluses) and n = 32 (solid black circles) of the 96 half-hour intervals corresponding to the different filters discussed, along with a thin dashed line at -47 ‰, the mean isotopic composition of ambient CH_4 in the free troposphere, and a thick dashed line at -71 ‰, the mean isotopic composition for n = 90 (gray triangles).

chamber due to emergent vegetation and/or inadequate mixing of the chamber headspace.

5. Results

[27] Figure 8 shows the mean mixing ratios of CH_4, CO_2, and $\delta^{13}C_{CH_4}$ along with relative humidity, temperature, u^*, wind speed, and wind direction. Half hour mean CH_4 and CO_2 mixing ratios were correlated, showing a diurnal pattern consistent with nighttime inversion of the Planetary Boundary Layer (PBL). These inversions typically involve stable atmospheric conditions, $u^* < 0.1$ m/s and low mean wind speeds. Wind direction averaged -35 degrees N-NW over the two days. Mean half-hourly $\delta^{13}C_{CH_4}$ values approached the free tropospheric northern hemisphere value of -47 ‰ during the periods of highest wind speed. During periods of lower mean wind speeds, the influence of the fen on the mean $\delta^{13}C_{CH_4}$ was apparent with deviations toward more ^{13}C depleted CH_4 values, consistent with a biogenic CH_4 source.

[28] The flux time series is shown in Figure 9 where solid dots represent fluxes calculated during periods in which u^* exceeded 0.1 m/s (fluxes for periods with $u^* < 0.1$ m/s are artifacts not used in our analysis but are shown as open gray circles). The mean CH_4 flux for the two days using only data with $u^* > 0.1$ m/s (solid dots) was 6.5 ± 0.7 (95% C.I.) mg CH_4 m^{-2} hr^{-1}, in excellent agreement with the mean autochamber CH_4 flux of 6.6 ± 0.8 (95% C.I.) mg CH_4 m^{-2} hr^{-1}. Mean CH_4 isofluxes were -518 ± 73 (95% C.I.) ‰ mg CH_4 m^{-2} hr^{-1} and the resulting distribution of inferred $\delta^{13}C_{CH_{4source}}$ had a mean of -79 ± 9 (95% C.I.) ‰.

[29] Figure 10 shows examples of chamber closing cycles illustrating the buildup of CH_4 following chamber closing at minute 1 and the abrupt return to near-ambient concentrations after minute 7 when the chamber opens (the lag is residual high CH_4 data from the closed QCLS loop not sampled during QCLS calibration). The linear regression to minutes 2–6 used to calculate the flux is shown in blue. High concentrations of CH_4 during the chamber closure intervals correspond to $\delta^{13}C_{CH_4}$ depletions, consistent with a biogenic CH_4 source. Keeling analysis is well suited to chamber data, as large enhancements from ambient concentrations of CH_4 that accumulate during a chamber closure improve regression statistics for extrapolation to infinite concentrations ($1/\chi_{CH_4} \to 0$) [*Pataki et al.*, 2003]. The linear increase in χ_{CH_4} shown in Figure 10 corresponds to a flux that is half the mean August fluxes yet still shows enhancements of ~ 1 μmol/mol above ambient CH_4 concentrations. The regression shown has a standard deviation on the intercept of 0.9 ‰, representing the error estimate of the isotopic source composition, $\delta^{13}C_{CH_{4source}}$. Uncertainties in the Keeling intercept decrease with increasing CH_4 enhancements, as shown in Figure 11. The 25, 50, and 75 quartiles of CH_4 fluxes have associated 1σ uncertainties on the isotopic source of 2.3 ‰, 1.6 ‰, and 1.1 ‰, with minimum uncertainties of <0.6 ‰ associated with the largest fluxes.

[30] Variability in Keeling intercepts largely represent real differences in the isotopic composition of CH_4 from the fen in the individual chambers. The distributions of $\delta^{13}C_{CH_{4source}}$ derived from EC isoflux methods and autochamber Keeling analysis are compared in Figure 12. Mean $\delta^{13}C_{CH_{4source}}$ from Keeling regressions (n = 332 chamber closings of linear and
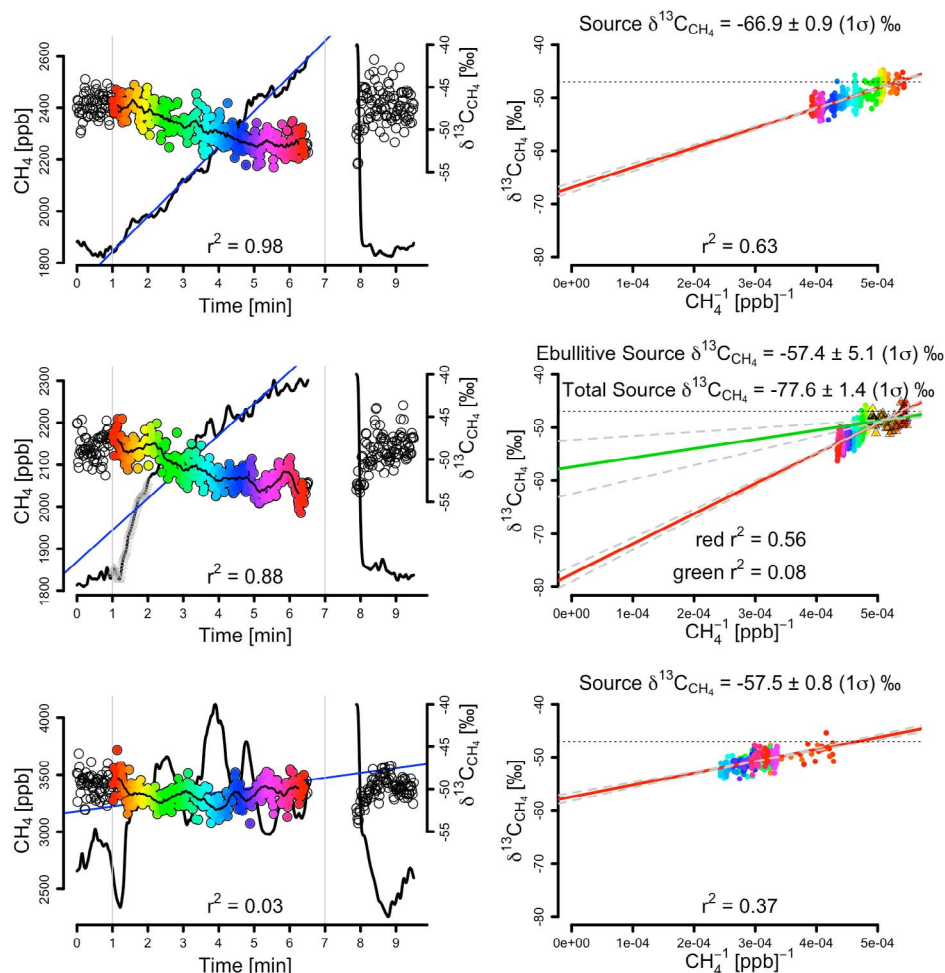
Figure 10. (left) Examples of QCLS autochamber subsampling intervals for (top) linear, (middle) ebullitive, and (bottom) random fluxes calculated with equation (9) and the blue regression. Missing data corresponds to background zero-air, low-span, or high-span calibration tank additions. (right) Corresponding Keeling plots for the three time series where $\delta^{13}C_{CH_4}$ is shown color-coded by elapsed time to relate the left plots to the right. The isotopic composition of background atmospheric CH_4 is shown at -47 ‰ (dotted black) and the Keeling regression slope is shown in red. An additional Keeling regression for an ebullition event (middle) is shown in green, where the gray (triangles) represent the ebullitive subset of the data used in the analysis.

ebullitive fluxes with q-statistic >0.5) was -64.5 ± 0.8 (95% C.I.) ‰, statistically indistinguishable (at p = 0.05) from -71 ± 8 (95% C.I.) ‰ for EC isoflux methods. Neither CH_4 fluxes nor $\delta^{13}C_{CH_{4source}}$ exhibited a significant diurnal pattern. Mean CH_4 fluxes for each of the individual 10 chambers highlighted the heterogeneity of the fen. Chambers with large percentages of *Carex* plants, for instance, had larger fluxes because plant mediated transport occurred faster than diffusion through surface water. The distributions of $\delta^{13}C_{CH_{4source}}$ by chamber, however, were statistically indistinguishable at p = 0.05.

6. Discussion

6.1. Error Estimates

[31] The precision of $^{12}CH_4$ and $^{13}CH_4$ compare well to other reported instrument precisions [*Hendriks et al.*, 2008; *Kroon et al.*, 2007; *Lee et al.*, 2009; *Nelson et al.*, 2004]. The

selection of spectral sampling features between 1294.1 and 1294.5 cm^{-1} combined with CW operation of a 30 mW QCL light source, a high D* thermoelectrically cooled 8 μm detector, and a 210 m effective path length resulted in a $\delta^{13}C_{CH_4}$ precision <0.2 ‰ at order 10^2 s averaging times. Reductions in isoflux error could be achieved with higher sampling rates accompanied by shorter sample cell residence times, and a more complete micrometeorological data set. We attribute 20% of our isoflux error to incomplete micrometeorological data, and estimate an upper limit on an improvement factor of ~2.2 ($\sqrt{5}$) for 5 Hz sampling. Recent improvements in cell design have resulted in a 2.1 L sampling cell volume with effective path lengths of up to 260 m using 554 passes between mirrors spaced ~47 cm apart where losses from mirror reflectivity due to higher pass numbers are mitigated by using wavelength specific mirror coatings [*McManus et al.*, 2011]. This reduced sampling volume would allow for independent sampling at ≥2 Hz and
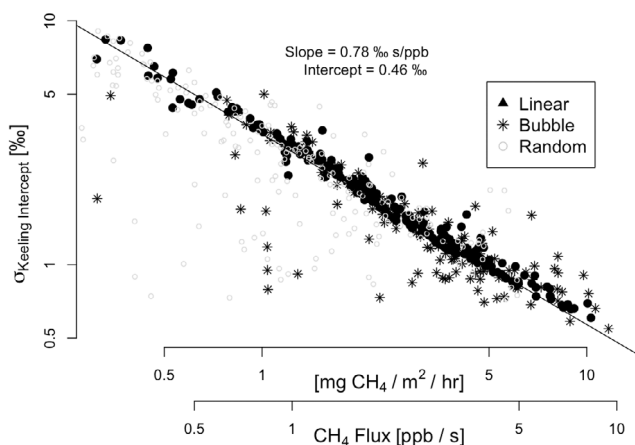
Figure 11. Log-log relationship of 1σ error on Keeling intercept as a function of CH_4 flux (shown with two separate but equivalent scales). The slope and intercept give predicted Keeling plot 1σ errors on the regression. The 1σ errors on the regression for linear, bubble, and random chamber build-ups are 1.3 ‰, 1.1 ‰, and 2.5 ‰, respectively. The variance is smaller on autochamber closings containing ebullitive events because excursions of CH_4 above ambient conditions are generally larger.

would decrease F_1, the high-frequency loss term of our EC measurements. It is hard to predict actual isoflux error improvements because 5 Hz measurement noise will also be ~ 2.2 ($\sqrt{5}$) times higher than that of 1 Hz sampling due to the acquisition of fewer spectra over a given sampling interval. The upper limit improvement with faster sampling

could decrease the standard deviation of the $\delta^{13}C_{CH_4}$ measurement distribution, $1\sigma_{\delta^{13}C_{CH_4}}$, from 25 ‰ to 9 ‰, approaching the real variability of the fen depicted in Figure 12 with the autochamber QCLS data.

[32] For comparison, the 1σ error estimate on F_{CH_4} was 0.97 mg CH_4 m^{-2} hr^{-1}, as calculated from the standard deviation of $\overline{w'\chi'_{CH_4}}$ for the first and last 20 s of a 100 s lag-time interval. This corresponded to a signal to noise (S/N) ratio of ~ 7. Smaller by a factor of two, the S/N of the isoflux was ~ 3.5 with a corresponding 1σ error estimate of 158 ‰ mg CH_4 m^{-2} hr^{-1} (or in alternate units, 66.4 ‰·nmol/mol·m/s). We characterized the error on the resultant $\delta^{13}C_{CH_{4source}}$ by dividing the isoflux error estimate by the range of mean CH_4 fluxes observed giving a mean $1\sigma_{\delta^{13}C_{CH_4}}$ of 25 ‰. This error is the same order as the deviation between the isotopic composition of CH_4 from the free troposphere (-47 ‰) and CH_4 from biogenic sources (-60 to -70 ‰) and illustrates how a decrease in the $1\sigma_{\delta^{13}C_{CH_4}}$ to 9 ‰ from a smaller sampling volume would improve the retrieved EC isoflux calculations.

6.2. CH_4 Fluxes

[33] Filtering of EC data by friction velocity is critical for EC systems [*Hendriks et al.*, 2008; *Kormann et al.*, 2001; *Wille et al.*, 2008]. Plotting CH_4 flux versus friction velocity shows that a drop in CH_4 flux occurs below u* values of 0.07 m/s at Sallie's Fen (auxiliary material Figure S1).[1] Other studies have used similar thresholds, notably 0.1 m/s [*Kormann et al.*, 2001] and 0.09 [*Hendriks et al.*, 2008]. We

---

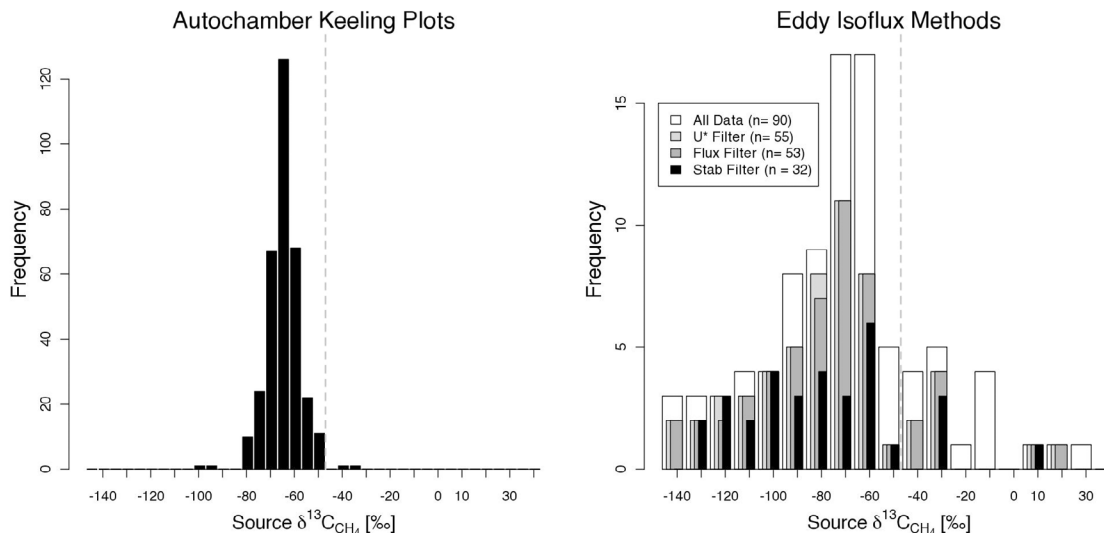[1]Auxiliary materials are available in the HTML. doi:10.1029/2011JD016960.

Figure 12. (left) Histogram of the $\delta^{13}C_{CH_{4source}}$ composition using autochamber Keeling plot methods. (right) Histogram of the half-hourly $\delta^{13}C_{CH_{4source}}$ composition calculated using EC isoflux methods. Of the 96 half-hour intervals, the 90 with isotopic composition within 3σ of the mean are shown in white and have a mean composition of -71 ‰. Filtering by u* > 0.1 m/s, CH_4 flux >1 nmol/mol-m/s, and stability parameter z/L $\in (-5,0)$ result in different mean isotopic composition of -79 ‰, -78 ‰, and -82 ‰. The 1σ of the distributions is 33 ‰ for all of the filters, similar to the isoflux measurement error derived from the cross covariance far from true lag-time. The gray vertical dashed line in both histograms represents the isotopic composition of atmospheric CH_4.

use 0.1 m/s as the threshold and note that only 6 half-hour points lie in the 0.07 to 0.1 range.

[34] Similar to *Hendriks et al.* [2008], we observed that mean CH_4 fluxes derived using vegetation-type-by-surface-area weighted fluxes of chamber data were statistically indistinguishable (at the p = 0.05 level) from EC measurements over the same period. Autochambers were distributed to be representative of the fen [*Bubier et al.*, 2003], and it is reassuring that the two methods produce similar CH_4 flux estimates. *Schuepp et al.* [1990] define a footprint function for fluxes in terms of local meteorological conditions and sampling height that predict a maximum surface sensitivity of the EC observations ~10 m upwind from the EC tower at Sallie's Fen, roughly 4 times smaller than the nearest edge of the fen. We estimate that 90% of the cumulative footprint lies within the area of the fen [*Kormann and Meixner*, 2000].

[35] Although we have only 10 days of measurements using the QCLS, yearlong autochamber measurements using the LGR show that seasonal trends in CH_4 emissions agree with those of similar fens [*Goodrich et al.*, 2011; *Rinne et al.*, 2007]. Flux magnitudes, in contrast to seasonality, are more site-dependent. Our mean CH_4 flux of 6.5 mg CH_4 m^{-2} hr^{-1} lie within the range of summertime fluxes observed at similar fens by *Hendriks et al.* [2008], *Rinne et al.* [2007], *Kormann et al.* [2001], and *Verma et al.* [1992], who report mean summertime emissions of 1.7, 3.5, 5.4, and 7.4 mg CH_4 m^{-2} hr^{-1}, respectively. With the exception of *Hendriks et al.* [2008], who report emission maximums during daytime, most studies do not observe diurnal patterns of CH_4 flux, suggesting that passive diffusion via plant vascular tissue is the dominant CH_4 transport mechanism to the atmosphere [*Chasar et al.*, 2000; *Popp et al.*, 1999; *Shannon et al.*, 1996].

[36] Differential attenuation of scalar measurements such as H_2O and CO_2 by closed-path EC systems must be accounted for when using WPL corrections [*Ibrom et al.*, 2007b]. Attenuation is particularly of concern for stable isotope measurements where there is potential for fractionation due to sampling. *Griffis et al.* [2008] characterize this sampling effect with a CO_2 isotope spectrometer and find attenuation <0.5 ‰ for both $\delta^{13}C_{CO_2}$ and $\delta^{18}O_{CO_2}$. We maintained fully turbulent conditions throughout our sampling system as fractionation has been demonstrated insignificant in turbulent conditions [*Griffis et al.*, 2008].

6.3. Isofluxes and $\delta^{13}C_{CH_{4source}}$

[37] CH_4 from anaerobic environments is released to the atmosphere largely by three different processes: diffusion through peatland pore water, plant mediated transport, and ebullition. Depth profiles of pore water CH_4 show that CO_2 reduction to CH_4 is the dominant pathway of methanogenesis at depth while acetate fermentation is more prevalent closer to the surface [*Popp et al.*, 1999, 2000]. At the oxic-anoxic interface, CH_4 oxidation results in ^{13}C enrichment because methanotrophs preferentially oxidize $^{12}CH_4$ by roughly 5–20 ‰ [*King et al.*, 1989; *Whiticar*, 1999]. Of the three transport pathways, ebullition is perhaps the most poorly quantified and least understood. *Goodrich et al.* [2011] estimated that ebullition accounted for up to 12% of CH_4 fluxes at Sallie's Fen by separating linear fluxes (pore water diffusion and plant-mediated fluxes) from ebullitive fluxes using the same methods described in section 4.3.

[38] Ebullition exhibited a diurnal cycle at Sallie's Fen, with more ebullitive events occurring at night [*Goodrich et al.*, 2011]. Keeling intercepts of ebullitive fluxes measured during the 8 days of QCLS subsampling were on average 1.2 ± 0.7 ‰ (95% C.I., $1\sigma = \pm$ 3.2 ‰) enriched in ^{13}C compared to the Keeling intercept using the entire chamber subset. We hypothesize that bubbles which can form and grow on plant vascular tissue are more likely to encounter more oxic conditions due to plant pathways that facilitate oxygen exchange. CH_4 oxidation to CO_2 leaves residual CH_4 in the bubble enriched in ^{13}C which can later outgas via ebullition. A complementary effect proposed by *Chanton et al.* [1997] is that plants relying on passive gas transport act as restrictive pipes that discriminate against ^{13}C. In rice paddies, this effect, combined with a fraction of total CH_4 being oxidized, produced what they refer to as 'bubble CH_4' enriched in ^{13}C by roughly 5 ‰ [*Chanton et al.*, 1997]. This diffusional fractionation, theoretically a 19.5 ‰ effect in air but a smaller effect in water, could also explain the observed difference as ebullitive fluxes originating from depth would tend to bypass diffusional fractionation in the water column [*Popp et al.*, 1999; *Cerling et al.*, 1991].

[39] The mean $\delta^{13}C_{CH_{4source}}$ calculated by bootstrapping using resampled data (1000 times, with replacement) to construct a population distribution of the Keeling plot autochamber analysis was −64.5 ± 0.8 (95% C.I.) ‰. This agrees with the isotopic content of CH_4 from similar ecosystems as presented by *Popp et al.* [1999, 2000] and *Whiticar* [1999]. Bootstrapped mean $\delta^{13}C_{CH_{4source}}$ by EC isoflux techniques were −71 ± 8 (95% C.I.) ‰, −79 ± 9 ‰, and −82 ± 12 ‰ using subsets of the total 96 half-hour intervals, representing n = 90 intervals with $\delta^{13}C_{CH_{4source}}$ within 3σ of the mean calculated $\delta^{13}C_{CH_{4source}}$, n = 55 intervals with u* > 0.1 m/s, and n = 32 intervals with the stability parameter z/L <0 [see *Kormann et al.*, 2001], respectively (Figure 12). Because the covariance terms in equations (4) and (5) contain the same scalar measurements (w' and χ'_{CH_4}), dividing the two equations to calculate $\delta^{13}C_{CH_{4source}}$ results in error cancellation such that the retrieved $\delta^{13}C_{CH_{4source}}$ distribution by EC is statistically indistinguishable (at p = 0.05) from the autochamber Keeling plot derived $\delta^{13}C_{CH_{4source}}$ distribution when all the data (n = 90) are used. When filters typically applied to EC data are used (e.g., n = 55 or n = 32 subsets), the retrieved $\delta^{13}C_{CH_{4source}}$ is distinguishable (at p = 0.05) from the Keeling plot derived $\delta^{13}C_{CH_{4source}}$, though we note that these filters preferentially remove nighttime data, thereby biasing the distribution toward depleted ^{13}C values by partially removing the influence of ^{13}C enriched nighttime ebullitive fluxes. In the present study, Keeling plots provide a more robust constraint on the real distribution of $\delta^{13}C_{CH_{4source}}$ from the fen as our EC isoflux sample size is limited and the isoflux error is similar in magnitude to the variability of the $\delta^{13}C_{CH_{4source}}$ distribution from 332 Keeling plot intercepts.

7. Conclusion

[40] We presented measurements using a QCLS capable of in situ $\delta^{13}C_{CH_4}$ precisions of 1.5 ‰ and <0.2 ‰ at 1 s and 10^2 second averaging times, respectively, demonstrating that

both EC isoflux methods and autochamber Keeling analysis achieve consistent characterization of $\delta^{13}C_{CH_{4source}}$, producing statistically indistinguishable CH_4 flux estimates. Fast-response in situ atmospheric $^{13}CH_4$ and $^{12}CH_4$ measurements can robustly quantify the distributions of $\delta^{13}C_{CH_{4source}}$ from various CH_4 sources and characterize seasonal changes in these distributions. They can also therefore provide additional constraint for modeling efforts that use atmospheric $\delta^{13}C_{CH_4}$ data to quantify emission sources in global inventories [*Allan et al.*, 2001; *Lassey et al.*, 2007]. Modeling efforts to date have shown limited improvements from using both $\delta^{13}C_{CH_4}$ and CH_4 data, as opposed to CH_4 data alone, largely because GG-C-IRMS instrumentation limitations make $\delta^{13}C_{CH_4}$ data very scarce [*Fletcher et al.*, 2004a, 2004b; *Bousquet et al.*, 2006].

[41] Longer time series of EC or flux chamber $^{12}CH_4$ and $^{13}CH_4$ measurements may elucidate the seasonal dependence of processes affecting CH_4 fluxes, particularly in regions such as the arctic [*Dlugokencky et al.*, 2009, 2011] which have diverse CH_4 sources potentially susceptible to large scale environmental changes. In this study of a *Sphagnum*-dominated fen in New Hampshire, we used a week of automatic flux chamber measurements to characterize the bulk isotopic composition of late-August CH_4 emissions. We observed $\delta^{13}C_{CH_4}$ enrichment of ebullitive fluxes at night, which may be related to changes in oxygen status near plant roots. Continuous data, including $\delta^{13}C_{CH_4}$, over a year from autochambers can potentially identify the biogeochemical drivers of changes in both CH_4 fluxes and their isotopic composition at various timescales.

References

Allan, W., M. R. Manning, K. R. Lassey, D. C. Lowe, and A. J. Gomez (2001), Modeling the variation of $\delta^{13}C$ in atmospheric methane: Phase ellipses and the kinetic isotope effect, *Global Biogeochem. Cycles*, *15*(2), 467–481, doi:10.1029/2000GB001282.

Baldocchi, D. D., and D. R. Bowling (2003), Modelling the discrimination of $^{13}CO_2$ above and within a temperate broad-leaved forest canopy on hourly to seasonal time scales, *Plant Cell Environ.*, *26*(2), 231–244, doi:10.1046/j.1365-3040.2003.00953.x.

Bousquet, P., et al. (2006), Contribution of anthropogenic and natural sources to atmospheric methane variability, *Nature*, *443*(7110), 439–443, doi:10.1038/nature05132.

Bousquet, P., et al. (2011), Source attribution of the changes in atmospheric methane for 2006–2008, *Atmos. Chem. Phys.*, *11*, 3689–3700, doi:10.5194/acp-11-3689-2011.

Bowling, D. R., D. E. Pataki, and J. R. Ehleringer (2003), Critical evaluation of micrometeorological methods for measuring ecosystem-atmosphere isotopic exchange of CO_2, *Agric. For. Meteorol.*, *116*(3–4), 159–179, doi:10.1016/S0168-1923(03)00006-6.

Bubier, J., P. Crill, A. Mosedale, S. Frolking, and E. Linder (2003), Peatland responses to varying interannual moisture conditions as measured by automatic CO_2 chambers, *Global Biogeochem. Cycles*, *17*(2), 1066, doi:10.1029/2002GB001946.

Carroll, P., and P. Crill (1997), Carbon balance of a temperate poor fen, *Global Biogeochem. Cycles*, *11*(3), 349–356, doi:10.1029/97GB01365.

Cerling, T. E., D. K. Solomon, J. Quade, and J. R. Bowman (1991), On the isotopic composition of carbon in soil carbon dioxide, *Geochim. Cosmochim. Acta*, *55*, 3403–3405, doi:10.1016/0016-7037(91)90498-T.

Chanton, J. P., G. J. Whiting, N. E. Blair, C. W. Lindau, and P. K. Bollich (1997), Methane emission from rice: Stable isotopes, diurnal variations, and CO_2 exchange, *Global Biogeochem. Cycles*, *11*(1), 15–27, doi:10.1029/96GB03761.

Chasar, L. S., J. P. Chanton, P. H. Glaser, and D. I. Siegel (2000), Methane concentration and stable isotope distribution as evidence of rhizospheric processes: Comparison of a fen and bog in the Glacial Lake Agassiz Peatland complex, *Ann. Bot.*, *86*(3), 655–663, doi:10.1006/anbo.2000.1172.

Crosson, E. R., et al. (2002), Stable isotope ratios using cavity ring-down spectroscopy: Determination of $^{13}C/^{12}C$ for carbon dioxide in human breath, *Anal. Chem.*, *74*(9), 2003–2007, doi:10.1021/ac025511d.

Dawson, T. E., S. Mambelli, A. H. Plamboeck, P. H. Templer, and K. P. Tu (2002), Stable isotopes in plant ecology, *Annu. Rev. Ecol. Syst.*, *33*, 507–559, doi:10.1146/annurev.ecolsys.33.020602.095451.

De Biévre, P., N. E. Holden, and I. L. Barnes (1984), Isotopic abundances and atomic weights of the elements, *J. Phys. Chem. Ref. Data*, *13*, 809–891, doi:10.1063/1.555720.

Dlugokencky, E. J., S. Houweling, L. Bruhwiler, K. A. Masarie, P. M. Lang, J. B. Miller, and P. P. Tans (2003), Atmospheric methane levels off: Temporary pause or a new steady-state?, *Geophys. Res. Lett.*, *30*(19), 1992, doi:10.1029/2003GL018126.

Dlugokencky, E. J., et al. (2009), Observational constraints on recent increases in the atmospheric CH_4 burden, *Geophys. Res. Lett.*, *36*, L18803, doi:10.1029/2009GL039780.

Dlugokencky, E. J., E. G. Nisbet, R. Fisher, and D. Lowry (2011), Global atmospheric methane: Budget, changes and dangers, *Philos. Trans. R. Soc. A*, *369*, 2058–2072, doi:10.1098/rsta.2010.0341.

Faist, J., F. Capasso, D. L. Sivco, C. Sirtori, A. L. Hutchinson, and A. Y. Cho (1994), Quantum cascade laser, *Science*, *264*(5158), 553–556, doi:10.1126/science.264.5158.553.

Fletcher, S. E. M., P. P. Tans, L. M. Bruhwiler, J. B. Miller, and M. Heimann (2004a), CH_4 sources estimated from atmospheric observations of CH_4 and its $^{13}C/^{12}C$ isotopic ratios: 1. Inverse modeling of source processes, *Global Biogeochem. Cycles*, *18*, GB4004, doi:10.1029/2004GB002223.

Fletcher, S. E. M., P. P. Tans, L. M. Bruhwiler, J. B. Miller, and M. Heimann (2004b), CH_4 sources estimated from atmospheric observations of CH_4 and its $^{13}C/^{12}C$ isotopic ratios: 2. Inverse modeling of CH4 fluxes from geographical regions, *Global Biogeochem. Cycles*, *18*, GB4005, doi:10.1029/2004GB002224.

Frolking, S., and P. Crill (1994), Climate controls on temporal variability of methane flux from a poor fen in southeastern New Hampshire: Measurement and modeling, *Global Biogeochem. Cycles*, *8*(4), 385–397, doi:10.1029/94GB01839.

Gierczak, T., R. K. Talukdar, S. C. Herndon, G. L. Vaghjiani, and A. R. Ravishankara (1997), Rate coefficients for the reactions of hydroxyl radicals with methane and deuterated methanes, *J. Phys. Chem. A*, *101*(17), 3125–3134, doi:10.1021/jp963892r.

Goodrich, J. P., R. K. Varner, S. Frolking, B. N. Duncan, and P. M. Crill (2011), High-frequency measurements of methane ebullition over a growing season at a temperate peatland site, *Geophys. Res. Lett.*, *38*, L07404, doi:10.1029/2011GL046915.

Griffis, T. J., S. D. Sargent, J. M. Baker, X. Lee, B. D. Tanner, J. Greene, E. Swiatek, and K. Billmark (2008), Direct measurement of biosphere-atmosphere isotopic CO_2 exchange using the eddy covariance technique, *J. Geophys. Res.*, *113*, D08304, doi:10.1029/2007JD009297.

Gupta, P., D. Noone, J. Galewsky, C. Sweeney, and B. H. Vaughn (2009), Demonstration of high-precision continuous measurements of water vapor isotopologues in laboratory and remote field deployments using wavelength-scanned cavity ring-down spectroscopy (WS-CRDS) technology, *Rapid Commun. Mass Spectrom.*, *23*(16), 2534–2542, doi:10.1002/rcm.4100.

Hendriks, D. M. D., A. J. Dolman, M. K. van der Molen, and J. van Huissteden (2008), A compact and stable eddy covariance set-up for methane measurements using off-axis integrated cavity output spectroscopy, *Atmos. Chem. Phys.*, *8*(2), 431–443, doi:10.5194/acp-8-431-2008.

Horst, T. W. (1997), A simple formula for attenuation of eddy fluxes measured with first-order-response scalar sensors, *Boundary Layer Meteorol.*, *82*, 219–233.

Ibrom, A., E. Dellwik, S. E. Larsen, and K. Pilegaard (2007a), On the use of the Webb-Pearman-Leuning theory for closed-path eddy correlation measurements, *Tellus, Ser. B*, *59*(5), 937–946, doi:10.1111/j.1600-0889.2007.00311.x.

Ibrom, A., E. Dellwik, H. Flyvbjerg, N. O. Jensen, and K. Pilegaard (2007b), Strong low-pass filtering effects on water vapour flux

measurements with closed-path eddy correlation systems, *Agric. For. Meteorol.*, *147*(3–4), 140–156, doi:10.1016/j.agrformet.2007.07.007.

Kaimal, J. C., and J. J. Finnigan (1994), *Atmospheric Boundary Layer Flows: Their Structure and Measurement*, Oxford Univ. Press, New York.

King, S. L., P. D. Quay, and J. M. Lansdown (1989), The $^{13}C/^{12}C$ kinetic isotope effect for soil oxidation of methane at ambient atmospheric concentrations, *J. Geophys. Res.*, *94*(D15), 18,273–18,277, doi:10.1029/89JD01592.

Knohl, A., and N. Buchmann (2005), Partitioning the net CO_2 flux of a deciduous forest into respiration and assimilation using stable carbon isotopes, *Global Biogeochem. Cycles*, *19*, GB4008, doi:10.1029/2004GB002301.

Kormann, R., and F. X. Meixner (2000), An analytical footprint model for non-neutral stratification, *Boundary Layer Meteorol.*, *99*, 207–224.

Kormann, R., H. Muller, and P. Werle (2001), Eddy flux measurements of methane over the fen "Murnauer Moos", 11°11′E, 47°39′N, using a fast tunable diode laser spectrometer, *Atmos. Environ.*, *35*(14), 2533–2544, doi:10.1016/S1352-2310(00)00424-6.

Kosterev, A. A., R. F. Curl, F. K. Tittel, C. Gmachl, F. Capasso, D. L. Sivco, J. N. Baillargeon, A. L. Hutchinson, and A. Y. Cho (1999), Methane concentration and isotopic composition measurements with a mid-infrared quantum-cascade laser, *Opt. Lett.*, *24*(23), 1762–1764, doi:10.1364/OL.24.001762.

Kroon, P. S., A. Hensen, H. J. J. Jonker, M. S. Zahniser, W. H. van 't Veen, and A. T. Vermeulen (2007), Suitability of quantum cascade laser spectroscopy for CH_4 and N_2O eddy covariance flux measurements, *Biogeosciences*, *4*(5), 715–728, doi:10.5194/bg-4-715-2007.

Lassey, K. R., D. C. Lowe, and M. R. Manning (2000), The trend in atmospheric methane $\delta^{13}C$ and implications for isotopic constraints on the global methane budget, *Global Biogeochem. Cycles*, *14*(1), 41–49, doi:10.1029/1999GB900094.

Lassey, K. R., D. M. Etheridge, D. C. Lowe, A. M. Smith, and D. F. Ferretti (2007), Centennial evolution of the atmospheric methane budget: What do the carbon isotopes tell us?, *Atmos. Chem. Phys.*, *7*(8), 2119–2139, doi:10.5194/acp-7-2119-2007.

Lee, X., W. Massman, and B. Law (2004), *Handbook of Micrometeorology: A Guide for Surface Flux Measurement and Analysis*, Kluwer Acad., Dordrecht, Netherlands.

Lee, X. H., T. J. Griffis, J. M. Baker, K. A. Billmark, K. Kim, and L. R. Welp (2009), Canopy-scale kinetic fractionation of atmospheric carbon dioxide and water vapor isotopes, *Global Biogeochem. Cycles*, *23*, GB1002, doi:10.1029/2008GB003331.

Lelieveld, J., P. J. Crutzen, and F. J. Dentener (1998), Changing concentration, lifetime and climate forcing of atmospheric methane, *Tellus, Ser. B*, *50*(2), 128–150, doi:10.1034/j.1600-0889.1998.t01-1-00002.x.

Lowe, D. C., C. A. M. Brenninkmeijer, S. C. Tyler, and E. J. Dlugokencky (1991), Determination of the isotopic composition of atmospheric methane and its application in the Antarctic, *J. Geophys. Res.*, *96*(D8), 15,455–15,467, doi:10.1029/91JD01119.

McManus, J. B., P. L. Kebabian, and W. S. Zahniser (1995), Astigmatic mirror multipass absorption cells for long-path-length-spectroscopy, *Appl. Opt.*, *34*(18), 3336–3348, doi:10.1364/AO.34.003336.

McManus, J. B., D. D. Nelson, J. H. Shorter, R. Jimenez, S. Herndon, S. Saleska, and M. Zahniser (2005), A high precision pulsed quantum cascade laser spectrometer for measurements of stable isotopes of carbon dioxide, *J. Mod. Opt.*, *52*(16), 2309–2321, doi:10.1080/09500340500303710.

McManus, J. B., D. D. Nelson, and M. S. Zahniser (2010), Long-term continuous sampling of $^{12}CO_2$, $^{13}CO_2$ and $^{12}C^{18}O^{16}O$ in ambient air with a quantum cascade laser spectrometer, *Isotopes Environ. Health Stud.*, *46*(1), 49–63, doi:10.1080/10256011003661326.

McManus, J. B., M. S. Zahniser, and D. D. Nelson (2011), Dual quantum cascade laser trace gas instrument with astigmatic Herriott cell at high pass number, *Appl. Opt.*, *50*(4), A74–A85, doi:10.1364/AO.50.000A74.

Melloh, R. A., and P. M. Crill (1996), Winter methane dynamics in a temperate peatland, *Global Biogeochem. Cycles*, *10*(2), 247–254, doi:10.1029/96GB00365.

Miller, J. B., K. A. Mack, R. Dissly, J. W. C. White, E. J. Dlugokencky, and P. P. Tans (2002), Development of analytical methods and measurements of $^{13}C/^{12}C$ in atmospheric CH_4 from the NOAA Climate Monitoring and Diagnostics Laboratory global air sampling network, *J. Geophys. Res.*, *107*(D13), 4178, doi:10.1029/2001JD000630.

Mohn, J., C. Guggenheim, B. Tuzson, M. K. Vollmer, S. Toyoda, N. Yoshida, and L. Emmenegger (2010), A liquid nitrogen-free preconcentration unit for measurements of ambient N_2O isotopomers by QCLAS, *Atmos. Meas. Tech.*, *3*(3), 609–618, doi:10.5194/amt-3-609-2010.

Montzka, S. A., M. Krol, E. Dlugokencky, B. Hall, P. Jöckel, and J. Lelieveld (2011), Small interannual variability of global atmospheric hydroxyl, *Science*, *331*, 67–69, doi:10.1126/science.1197640.

Nelson, D. D., J. H. Shorter, J. B. McManus, and M. S. Zahniser (2002), Sub-part-per-billion detection of nitric oxide in air using a thermoelectrically cooled mid-infrared quantum cascade laser spectrometer, *Appl. Phys. B*, *75*, 343–350, doi:10.1007/s00340-002-0979-4.

Nelson, D. D., B. McManus, S. Urbanski, S. Herndon, and M. S. Zahniser (2004), High precision measurements of atmospheric nitrous oxide and methane using thermoelectrically cooled mid-infrared quantum cascade lasers and detectors, *Spectrochim. Acta, Part A*, *60*(14), 3325–3335, doi:10.1016/j.saa.2004.01.033.

Pataki, D. E., J. R. Ehleringer, L. B. Flanagan, D. Yakir, D. R. Bowling, C. J. Still, N. Buchmann, J. O. Kaplan, and J. A. Berry (2003), The application and interpretation of Keeling plots in terrestrial carbon cycle research, *Global Biogeochem. Cycles*, *17*(1), 1022, doi:10.1029/2001GB001850.

Popp, T. J., J. P. Chanton, G. J. Whiting, and N. Grant (1999), Methane stable isotope distribution at a Carex dominated fen in north central Alberta, *Global Biogeochem. Cycles*, *13*(4), 1063–1077, doi:10.1029/1999GB900060.

Popp, T. J., J. P. Chanton, G. J. Whiting, and N. Grant (2000), Evaluation of methane oxidation in the rhizosphere of a Carex dominated fen in north central Alberta, Canada, *Biogeochemistry*, *51*(3), 259–281, doi:10.1023/A:1006452609284.

Press, W. H., S. A. Teukolsky, W. T. Vetterling, and B. P. Flannery (1992), *Numerical Recipes in C: The Art of Scientific Computing*, 2nd ed., Cambridge Univ. Press, New York.

Quay, P., J. Stutsman, D. Wilbur, A. Snover, E. Dlugokencky, and T. Brown (1999), The isotopic composition of atmospheric methane, *Global Biogeochem. Cycles*, *13*(2), 445–461, doi:10.1029/1998GB900006.

Rigby, M., et al. (2008), Renewed growth of atmospheric methane, *Geophys. Res. Lett.*, *35*, L22805, doi:10.1029/2008GL036037.

Rinne, J., T. Riutta, M. Pihlatie, M. Aurela, S. Haapanala, J. P. Tuovinen, E. S. Tuittila, and T. Vesala (2007), Annual cycle of methane emission from a boreal fen measured by the eddy covariance technique, *Tellus, Ser. B*, *59*(3), 449–457, doi:10.1111/j.1600-0889.2007.00261.x.

Saleska, S. R., J. H. Shorter, S. Herndon, R. Jimenez, B. McManus, J. W. Munger, D. D. Nelson, and M. S. Zahniser (2006), What are the instrumentation requirements for measuring the isotopic composition of net ecosystem exchange of CO_2 using eddy covariance methods?, *Isotopes Environ. Health Stud.*, *42*(2), 115–133, doi:10.1080/10256010600672959.

Saueressig, G., J. N. Crowley, P. Bergamaschi, C. Bruhl, C. A. M. Brenninkmeijer, and H. Fischer (2001), Carbon 13 and D kinetic isotope effects in the reactions of CH_4 with $O(^1D)$ and OH: New laboratory measurements and their implications for the isotopic composition of stratospheric methane, *J. Geophys. Res.*, *106*(D19), 23,127–23,138, doi:10.1029/2000JD000120.

Schuepp, P. H., M. Y. Leclerc, J. I. Macpherson, and R. L. Desjardins (1990), Footprint prediction of scalar fluxes from analytical solutions of the diffusion equation, *Boundary Layer Meteorol.*, *50*(1–4), 353–373.

Shannon, R. D., J. R. White, J. E. Lawson, and B. S. Gilmour (1996), Methane efflux from emergent vegetation in peatlands, *J. Ecol.*, *84*(2), 239–246, doi:10.2307/2261359.

Shoemaker, J. K., and D. P. Schrag (2010), Subsurface characterization of methane production and oxidation from a New Hampshire wetland, *Geobiology*, *8*, 234–243, doi:10.1111/j.1472-4669.2010.00239.x.

Smeets, C. J., R. Holzinger, I. Vigano, A. H. Goldstein, and T. Rockmann (2009), Eddy covariance methane measurements at a Ponderosa pine plantation in California, *Atmos. Chem. Phys.*, *9*(21), 8365–8375, doi:10.5194/acp-9-8365-2009.

Treat, C. C., J. L. Bubier, R. K. Varner, and P. M. Crill (2007), Timescale dependence of environmental and plant-mediated controls on CH_4 flux in a temperate fen, *J. Geophys. Res.*, *112*, G01014, doi:10.1029/2006JG000210.

Tuzson, B., J. Mohn, M. J. Zeeman, R. A. Werner, W. Eugster, M. S. Zahniser, D. D. Nelson, J. B. McManus, and L. Emmenegger (2008), High precision and continuous field measurements of $\delta^{13}C$ and $\delta^{18}O$ in carbon dioxide with a cryogen-free QCLAS, *Appl. Phys. B*, *92*(3), 451–458, doi:10.1007/s00340-008-3085-4.

Tuzson, B., R. V. Hiller, K. Zeyer, W. Eugster, A. Neftel, C. Ammann, and L. Emmenegger (2010), Field intercomparison of two optical analyzers for CH_4 eddy covariance flux measurements, *Atmos. Meas. Tech.*, *3*, 1519–1531, doi:10.5194/amt-3-1519-2010.

Verma, S. B., F. G. Ullman, D. Billesbach, R. J. Clement, J. Kim, and E. S. Verry (1992), Eddy-correlation measurements of methane flux in a northern peatland ecosystem, *Boundary Layer Meteorol.*, *58*(3), 289–304, doi:10.1007/BF02033829.

Waechter, H., J. Mohn, B. Tuzson, L. Emmenegger, and M. W. Sigrist (2008), Determination of N_2O isotopomers with quantum cascade laser based absorption spectroscopy, *Opt. Express*, *16*(12), 9239–9244, doi:10.1364/OE.16.009239.

Webb, E. K., G. I. Pearman, and R. Leuning (1980), Correction of flux measurements for density effects due to heat and water-vapor transfer, *Q. J. R. Meteorol. Soc.*, *106*(447), 85–100, doi:10.1002/qj.49710644707.

Whiticar, M. J. (1999), Carbon and hydrogen isotope systematics of bacterial formation and oxidation of methane, *Chem. Geol.*, *161*(1–3), 291–314, doi:10.1016/S0009-2541(99)00092-3.

Wienhold, F. G., H. Frahm, and G. W. Harris (1994), Measurements of N_2O fluxes from fertilized grassland using a fast response tunable diode laser spectrometer, *J. Geophys. Res.*, *99*(D8), 16,557–16,567, doi:10.1029/93JD03279.

Wille, C., L. Kutzbach, T. Sachs, D. Wagner, and E. M. Pfeiffer (2008), Methane emission from Siberian arctic polygonal tundra: Eddy covariance measurements and modeling, *Global Change Biol.*, *14*(6), 1395–1408, doi:10.1111/j.1365-2486.2008.01586.x.

Witinski, M., D. S. Sayres, and J. G. Anderson (2011), High precision methane isotopologue ratio measurements at ambient mixing ratios using integrated cavity output spectroscopy, *Appl. Phys. B*, *102*(2), 375–380, doi:10.1007/s00340-010-3957-2.

Zahniser, M. S., D. D. Nelson, J. B. McManus, and P. L. Kebabian (1995), Measurement of trace gas fluxes using tunable diode-laser spectroscopy, *Philos. Trans. R. Soc. A*, *351*(1696), 371–381.

Zahniser, M. S., et al. (2009), Infrared QC laser applications to field measurements of atmospheric trace gas sources and sinks in environmental research: Enhanced capabilities using continuous wave QCLs, *Proc. SPIE Int. Soc. Opt. Eng.*, *7222*, 7222OH, doi:10.1117/12.815172.